

Numerical simulation of heat transfer and fluid flow in GTA/Laser hybrid welding

B. Ribic, R. Rai and T. DebRoy

In order to understand the temperature fields, cooling rates and mixing in the weld pool, a comprehensive, three-dimensional heat transfer and fluid flow model is developed and tested by comparing model predictions with two sets of experimental data. The first set of data was taken from the literature. The experiments varied the separation distance between the heat sources for three arc current levels at a constant laser power. The second set of experiments analysed the effect of varying laser power for a constant heat source separation distance. The results demonstrate that the distance between the two heat sources significantly affects the cooling rates. The calculated results showed that the hybrid weld pool was very well mixed with strong convection currents resulting from the interaction between the electromagnetic and Marangoni forces. The calculated and experimental results showed that hybrid welding increases the weld pool width and gap bridgability when compared with laser welding. The weld pool depth in hybrid welding was affected mainly by the characteristics of the laser beam. Hybrid weld pool penetration depth is maximised at an optimal distance between the arc electrode and laser beam. The cooling rate increases significantly when the heat sources are separated beyond a critical distance. At close separation between arc and laser, calculations show that the arc radius must be decreased to achieve the observed weld depths.

Keywords: Hybrid welding, Heat transfer and fluid flow, Laser beam, Gas tungsten arc, Modeling, Cooling rate, Keyhole

Introduction

Hybrid welding involves the joining of metals and alloys by a laser beam and electrical arc. The hybrid welding process incorporates the benefits of both laser and arc welding in order to overcome their individual problems.^{1–6} Figure 1 is a schematic of the laser/GTAW hybrid welding process, which depicts the heat source separation distance and arc angle and length. The laser beam, with energy density greater than 10^9 W m^{-2} , provides relatively deep penetration at high welding velocities without the necessity of additional passes.^{1–10} The hybrid welding process results in less residual stress and thermal distortion compared to arc welding. Gap tolerance is also increased due to the generation of a wide weld pool.^{1–6} Experimental research has also shown that hybrid welding can reduce the propensity of cracking and presence of brittle phases due to relatively lower cooling rates.^{11–14} Furthermore, keyhole stability increases, which reduces the amount of porosity due to unstable keyhole collapse.^{12,15–18}

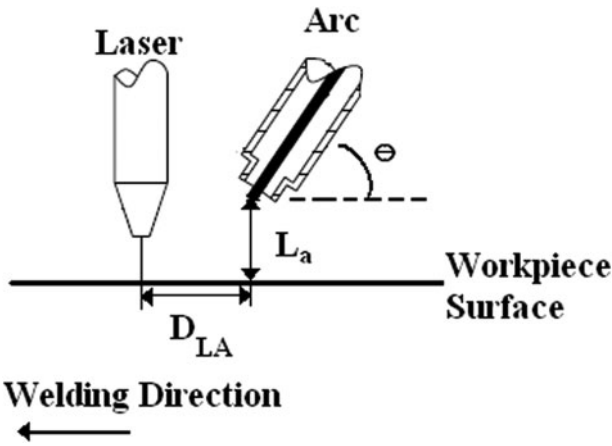
The experimentally observed benefits of hybrid welding are due to the interaction of the laser and arc heat

sources.^{1,2,4–6,19–21} When the arc and laser focal points are within close proximity, the heat sources may interact.^{2,5,19,20} The interaction of the two heat sources during hybrid welding is explained by two phenomena. First, arc stability is enhanced due to the introduction of metal vapours into the arc plasma from the laser induced keyhole.^{2,5,8–10,19,20,22–33} The metal vapours increase the electrical conductivity of the arc plasma.^{2,5,19,20,22,24,26,27,32,33} In addition, the arc contracts, causing an increase in current density.^{2,22,24,26,27,34} In the case of introducing copper vapours into a free burning arc, it was observed that the current density can increase by a factor of four.²⁶ Depending on the separation distance between the heat sources, the arc can bend towards the laser generated keyhole, rooting closer than the physical separation distance.^{2,19,20,26}

Beyond a critical separation distance, the arc is unable to bend or root on the keyhole due to the lack of metal vapour introduced to the arc plasma, explaining why the effect decreases as the distance between the two heat sources increases.^{2,5,19,20} Chen *et al.*² experimentally studied the hybrid welding of AISI 321 stainless steel and observed the laser–arc interaction. They did not credit the observed effects to any particular phenomena, but described that a particular value of separation between the two heat sources resulted in a relatively small increase in the penetration of the weld pool. Chen

Department of Materials Science and Engineering, The Pennsylvania State University, 115 Steidle Building, University Park, PA, 16802, US

*Corresponding author, email debroy@psu.edu



1 Schematic of laser/GTAW hybrid welding process: in this case, laser is leading, D_{LA} is separation distance between arc electrode and laser focal point, L_a is arc length or vertical separation distance between arc electrode and workpiece surface, and θ is arc angle relative to workpiece surface

et al.² also observed, with the aid of a camera, that for relatively small separation distance, the arc appeared to focus down inside the keyhole of the weld pool throughout the welding process.²

Several experimental studies^{2,3,5,6,11-13,19,20,25,35-56} have firmly established the benefits of hybrid welding. However, much of the process details have not been revealed. Very few numerical studies⁵⁷⁻⁵⁹ have been conducted on the physical processes of hybrid welding. Chen et al.⁵⁷ calculated the temperature fields in CO₂ laser/GTAW hybrid welding using a heat conduction based finite element model. Cho and Farson⁵⁸ utilised a three-dimensional heat transfer and fluid flow model to evaluate the humping defect formation in CO₂ laser/GMAW hybrid welding. Zhou et al.⁵⁹ studied the temperature fields and mixing of filler metal in laser/GMAW hybrid welding using a three-dimensional fluid flow and heat transfer model.

In this work, the authors study the quantitative role of arc radius and heat source separation distance and the arc constriction on the heat transfer and fluid flow, and verify the validity of the developed hybrid welding code. A three-dimensional fluid flow and heat transfer model is proposed to study the effect of heat source separation distance on weld geometry and cooling rates for hybrid welding experiments performed by Chen et al.² Furthermore, hybrid welding experiments were performed in order to understand the role of laser power level. The welds were made using a Nd:YAG laser heat source of nominal power levels of 0.8, 1.9, 3.8, and 4.5 kW. The arc heat source was a GTA operating at approximately 191 A and 11 V. The temperature field and fluid flow were studied for GTAW, laser welding and hybrid welding and the computed weld geometries were compared to experimental results.

Mathematical model

Calculation of keyhole profile

The keyhole geometry is calculated based on energy balance on keyhole walls.^{60,61} Keyhole walls are assumed to be at the boiling point of the alloy. Due to the significantly higher temperature gradient in any

direction in the horizontal plane compared to the vertical direction, planar heat conduction is assumed. The salient features of the model are presented in Appendix.

The calculated temperature distribution from the keyhole model is stored in a data file with all temperatures inside the keyhole assigned the boiling point temperature. This file is read in the thermofluid model and all points with the boiling point are considered within the keyhole. At each horizontal xy plane, the keyhole boundary is identified by a minimum and a maximum x value for any y value.

Heat transfer in weld pool

After calculating the keyhole profile, equations of conservation of mass, momentum, and energy are solved in three dimensions. The liquid metal flow in the weld pool can be represented by the following momentum conservation equation^{10,62,63}

$$\rho \frac{\partial u_i}{\partial t} + \rho \frac{\partial(u_i u_j)}{\partial x_j} = \frac{\partial}{\partial x_i} \left(\mu \frac{\partial u_j}{\partial x_i} \right) + S_j \quad (1)$$

where ρ is the density, t is the time, x_i is the distance along the i th ($i=1, 2$ and 3) orthogonal direction, u_j is the velocity component along the j direction, μ is the effective viscosity, and S_j is the source term for the j th momentum equation and is given as¹⁰

$$S_j = - \frac{\partial p}{\partial x_j} + \frac{\partial}{\partial x_i} \left(\mu \frac{\partial u_i}{\partial x_j} \right) - C \left(\frac{(1-f_L)^2}{f_L^3 + B} \right) u_j + \rho g_j \beta (T - T_{ref}) - \rho U \frac{\partial u_j}{\partial x_1} \quad (2)$$

where p represents the pressure, U is the welding velocity, and β is the coefficient of volume expansion. The third term represents the frictional dissipation in the mushy zone according to the Carman-Kozeny equation for flow through a porous media,^{64,65} where f_L is the liquid fraction, B is a very small computational constant introduced to avoid division by zero, and C is a constant accounting for the mushy zone morphology (a value of 1.6×10^4 was used in the present study⁶⁶). The fourth term is the buoyancy source term.⁶⁶⁻⁶⁸ The last term accounts for the motion of workpiece relative to the heat sources.⁶⁸

The following continuity equation is solved in conjunction with the momentum equation to obtain the pressure field

$$\frac{\partial(\rho u_i)}{\partial x_i} = 0 \quad (3)$$

In order to trace the weld pool liquid/solid interface, i.e. the phase change, the total enthalpy H is represented by a sum of sensible heat h and latent heat content ΔH , i.e. $H = h + \Delta H$.⁶⁹ The sensible heat h is expressed as $h = \int C_p dT$, where C_p is the specific heat, and T is the temperature. The latent heat content ΔH is given as $\Delta H = f_L L$, where L is the latent heat of fusion. The liquid fraction f_L is assumed to vary linearly with temperature for simplicity⁶⁸

$$f_L = \begin{cases} 1 & T > T_L \\ \frac{T - T_S}{T_L - T_S} & T_S \leq T \leq T_L \\ 0 & T < T_S \end{cases} \quad (4)$$

where T_L and T_S are the liquidus and solidus temperature respectively. Thus, the thermal energy transportation in the

weld workpiece can be expressed by the following modified energy equation¹⁰

$$\rho \frac{\partial h}{\partial t} + \rho \frac{\partial(u_i h)}{\partial x_i} = \frac{\partial}{\partial x_i} \left(\frac{k}{C_p} \frac{\partial h}{\partial x_i} \right) + S_h \quad (5)$$

where k is the thermal conductivity. The source term S_h is due to the latent heat content and is given as¹⁰

$$S_h = -\rho \frac{\partial(\Delta H)}{\partial t} - \rho \frac{\partial(u_i \Delta H)}{\partial x_i} - \rho U \frac{\partial h}{\partial x_1} - \rho U \frac{\partial \Delta H}{\partial x_1} \quad (6)$$

The heat transfer and fluid flow equations were solved for the complete workpiece. For the region inside the keyhole, the coefficients and source terms in the equations were adjusted to obtain boiling point temperature and zero fluid velocities.

Boundary conditions

A 3D Cartesian coordinate system is used in the calculation. Since the weld is symmetrical about the weld centreline, only half of the workpiece is considered. These boundary conditions are further discussed as follows.

Top surface

The weld top surface is assumed to be flat. The velocity boundary condition is given as^{70–73}

$$\begin{aligned} \mu \frac{\partial u}{\partial z} &= f_L \frac{d\gamma}{dT} \frac{\partial T}{\partial x} \\ \mu \frac{\partial v}{\partial z} &= f_L \frac{d\gamma}{dT} \frac{\partial T}{\partial y} \\ w &= 0 \end{aligned} \quad (7)$$

where u , v and w are the velocity components along the x , y and z directions respectively, and $d\gamma/dT$ is the temperature coefficient of surface tension. Since there is no outward flow at the pool top surface, the w velocity is zero.

The heat flux at the top surface is given as

$$\begin{aligned} k \frac{\partial T}{\partial z} \Big|_{\text{top}} &= \\ \frac{f_1 Q \eta_1}{\pi r_1^2} \exp \left[-\frac{f_1 (x_1^2 + y^2)}{r_1^2} \right] &+ \frac{f_a IV \eta_a}{\pi r_a^2} \exp \left[-\frac{f_a (x_a^2 + y^2)}{r_a^2} \right] \\ -\sigma \varepsilon (T^4 - T_a^4) - h_c (T - T_a) & \end{aligned} \quad (8)$$

where f_1 and f_a are the laser and arc power distribution factors respectively, Q is the total laser power, η_1 is the absorptivity, η_a is the arc efficiency, r_1 and r_a are the laser and arc radius respectively, x_1 and x_a are the location relative to the laser and arc respectively, I is the arc current, V is the arc voltage, σ is the Stefan-Boltzmann constant, h_c is the heat transfer coefficient, and T_a is the ambient temperature. In equation (8), the first and the second terms on the RHS are the heat input from the heat source, defined by a Gaussian heat distributions. The third and fourth terms represent the heat loss by radiation and convection respectively.

Symmetric plane

The boundary conditions are defined as zero flux across the symmetric surface, i.e. the vertical plane containing the welding direction, as¹⁰

$$\frac{\partial u}{\partial y} = 0, \quad v = 0, \quad \frac{\partial w}{\partial y} = 0 \quad (9)$$

$$\frac{\partial h}{\partial y} = 0 \quad (10)$$

Keyhole surface

$$h = h_{\text{boil}} \quad (11)$$

where h_{boil} is the sensible heat of the steel at its boiling point. This represents that the keyhole surface is at the boiling temperature. The velocity component perpendicular to the keyhole surface is assigned zero to represent no mass flux due to convection.

Bottom surface

For partial penetration welds, a convective heat transfer boundary condition, with a specified heat transfer coefficient, is given. Since the weld pool does not extend to the bottom, the velocities are zero at the bottom surface.

Solid surfaces

At all solid surfaces far away from the heat source, temperatures are set at ambient temperature (T_a) and the velocities are set to be zero.

Turbulence model

During keyhole mode laser welding, the rates of the transport of heat, mass and momentum are often enhanced because of the presence of fluctuating velocities in the weld pool. The contribution of the fluctuating velocities is considered by an appropriate turbulence model that provides a systematic framework for calculating effective viscosity and thermal conductivity.^{10,74,75} The values of these properties vary with the location in the weld pool and depend on the local characteristics of the fluid flow. In this work, a turbulence model based on Prandtl's mixing length hypothesis is used to estimate the turbulent viscosity¹⁰

$$\mu_t = \rho l_m v_t \quad (12)$$

where μ_t is the turbulent viscosity, l_m is the mixing length, and v_t is the turbulence velocity. Turbulence velocity can be estimated from the turbulent kinetic energy. Assuming turbulent kinetic energy to be about 10% of the mean kinetic energy, the turbulent velocity is approximately 30% of the mean velocity. Thus, the turbulent viscosity becomes¹⁰

$$\mu_t = 0.3 \rho l_m v \quad (13)$$

The corresponding local turbulent thermal conductivity, μ_{kt} is calculated from the turbulent Prandtl number, defined as $Pr = \frac{\mu_t c_p}{k_t}$, to be 0.9. Effective viscosity at a particular point is given as the sum of the turbulent (μ_t) and laminar (μ_l) viscosities, i.e. $\mu = \mu_t + \mu_l$.¹⁰

Experimental procedure

CO₂ laser/GTAW hybrid welding with the laser leading was performed by Chen *et al.*² on 4 mm thick AISI 321 stainless steel. The chemistry of the material was taken from standard commercial values given by Table 1. During the hybrid welding experiments, the distance between the arc electrode and laser beam was varied. The experiment was repeated for three arc current levels with the laser at sharp focus. The laser beam radius,

welding velocity, and laser power were 100 μm , 16.7 mm s^{-1} (1 m min^{-1}) and 900 W respectively. The arc voltage was 14 V and various arc currents were used including: 60, 120 and 180 A. The arc length and angle relative to the workpiece surface were 5.0 mm and 70° respectively. The arc was tilted backwards relative to the laser head, i.e. 30° relative to the normal. The separation distance between the heat sources was varied from 3.5 to approximately 9.2 mm. The photographic results of Chen *et al.* showed that for a 60 A arc, the arc and laser formed two separate plasma plumes at different locations on the welded surface when the distance of separation between the two sources was greater than the critical value of 6.48 mm. However, the published observations did not include the critical distance for the 120 and 180 A cases. Based on a parametric study on the effects of heat source separation and arc radius on weld penetrations, it was assumed that the heat sources acted at the same location for the 120 and 180 A cases for all of the separation distances studied.

Second, bead-on-plate Nd:YAG laser/GTAW hybrid, laser and arc welding was performed on 10 mm thick A131 structural steel at 8.5 mm s^{-1} . Table 2 shows the chemical composition of the A131 structural steel samples determined using atomic emission spectroscopy. The separation distance between the heat sources was 3.0 mm. The laser and hybrid welding laser power levels

Table 1 Chemical composition of AISI 321 stainless steel samples

Element	C	Cr	Mn	Mo	Ni	Fe	P	S	Ti	Si
Amount, wt-%	0.08	18.0	2.0	1.0	11.0	66.0	–	–	0.5	1.0

Table 2 Chemical composition of A131 structural steel samples

Element	C	Cr	Cu	Mn	Mo	Ni	P	S	Ti	V
Amount, wt-%	0.06	0.02	0.02	1.38	0.01	0.02	0.01	0.004	0.02	0.05

Table 3 Measured hybrid welding arc current and voltage values and their corresponding laser power levels: arc current and voltage were not constant for various hybrid welding cases

Weld type	Welding velocity, mm s^{-1}	Arc voltage, V	Arc current, A	Laser power, W
Hybrid	8.47	12.3	190	4500
		10.3	191	3800
		20	185	1900
		11	191	800

Table 4 Material properties used in welding calculations for AISI 321 stainless and A131 structural steels

Property	A131 structural steel	AISI 321 stainless steel
Density, kg m^{-3}	7000	7000
Solidus temperature, K (Ref. 10)	1745	1673
Liquidus temperature, K (Ref. 10)	1785	1723
Enthalpy of solid at melting point, J kg^{-1} (Ref. 10)	1.20E+06	1.20E+06
Enthalpy of liquid at melting point, J kg^{-1} (Ref. 10)	1.26E+06	1.26E+06
Specific heat of solid, $\text{J kg}^{-1} \text{K}^{-1}$ (Ref. 10)	711	711
Specific heat of liquid, $\text{J kg}^{-1} \text{K}^{-1}$ (Ref. 10)	795	795
Thermal conductivity of solid, J mKs^{-1} (Refs. 10 and 84)	29.3	20.9
Thermal conductivity of liquid J mKs^{-1} (Refs. 10 and 84)	29.3	29.3
Coefficient of thermal expansion, 1K^{-1} (Refs. 10 and 84)	1.96E-05	1.96E-05
Emissivity	0	0
$d\gamma/dT$ of pure material, N mK^{-1} (Refs. 10 and 84)	-0.00049	-0.00049
Concentration of surface active species, wt-%	0.004	0.0
Surface excess at saturation, mole m^{-2} (Ref. 85)	1.30E-05	1.30E-05
Enthalpy of segregation, J mol^{-1} (Ref. 85)	-1.66E+05	-1.66E+05
Entropy factor (Ref. 85)	0.00318	0.00318

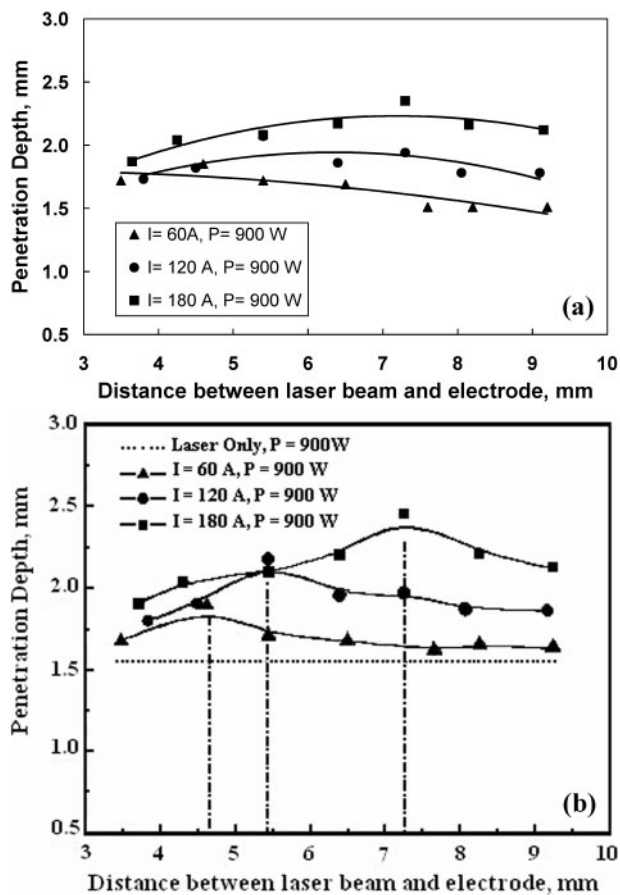
were 800, 1900, 3800 and 4500 W with a 12% loss in power assumed due to the laser optics and delivery.^{9,76} The laser was at sharp focus and had a beam radius of 250 μm . The lone GTAW voltage and current were 11 V and 191 A respectively. The arc current and voltage were not constant for the hybrid welding experiments. The arc was applied at a 45° angle relative to the normal and the arc length was approximately 1.5 mm. Table 3 shows the measured arc current and voltages for the various hybrid welding cases. The material properties used in order to complete the welding calculations for AISI 321 stainless and A131 structural steels are given in Table 4.

Results and discussion

The role of heat source separation distance on weld pool geometry and cooling rate

According to Chen *et al.*,² when the separation distance between the heat sources was greater than 6.5 mm, two separate plasma plumes were observable for hybrid welding conducted with a 60 A arc. In this case, the welding performed was a tandem process. During tandem welding, the arc primarily acts as a post heat treatment, which significantly decreases the cooling rate of the weld pool material.

When the separation distance between the heat sources was less than 6.5 mm for the 60 A arc hybrid welding case, arc bending caused the heat sources to act at the same location. When not under the influence of metal vapours generated by the laser beam, the arc radius for a 60 A arc is approximately 4.2 mm, which is based on the work of Tsai and Eager⁷⁷ on the distribution of heat and current fluxes in gas tungsten arcs. It was assumed that 95% of the arc current density



2 Penetration depth of hybrid welding of AISI 321 stainless steel samples as function of distance between laser beam and arc electrode and current of arc heat source: laser power level was 900 W for all welding cases; welding velocity was 16.7 mm s^{-1} for all welds; arc current levels were 60, 120 and 180 A; dashed horizontal line is penetration depth achieved by lone laser welding; a calculated result b experimental measured result²

distribution would fall within a circular radius of $r=6^{1/2}\sigma_I$, where σ_I is the current density distribution parameter.⁷⁷ The current density distribution parameter was selected based on the arc length and angle.⁷⁷

In the case of the 120 and 180 A arcs, the arc radii are 5.5 and 6.1 mm respectively, when not under the influence of metal vapours. It was observed that for the range of separation distances considered in this experiment, the calculated penetration depth did not change significantly when a constant arc radius was used. In addition, the calculated penetration depth obtained by use of the arc radii predicted from the

results of Tsai and Eager did not result in the penetration depth observed by Chen *et al.*, even when the separation distance was zero. Therefore, it was assumed that the heat source plasmas interacted for all of the separation distances during the 120 and 180 A arc hybrid welds despite the increase in separation distance between the electrode and laser beam. Table 5 shows the arc radii values necessary in order to calculate the observed results of Chen *et al.*² Calculations were made assuming that the arc was constricted because of the arc–laser interaction. In order to achieve the experimentally observed weld pool depths, the arc radius was reduced to account for arc contraction. Table 5 shows that the arc radius decreases to a minimum value at an optimal separation distance. Further investigation is needed to understand how the separation distance affects the plasma interaction in hybrid welding.

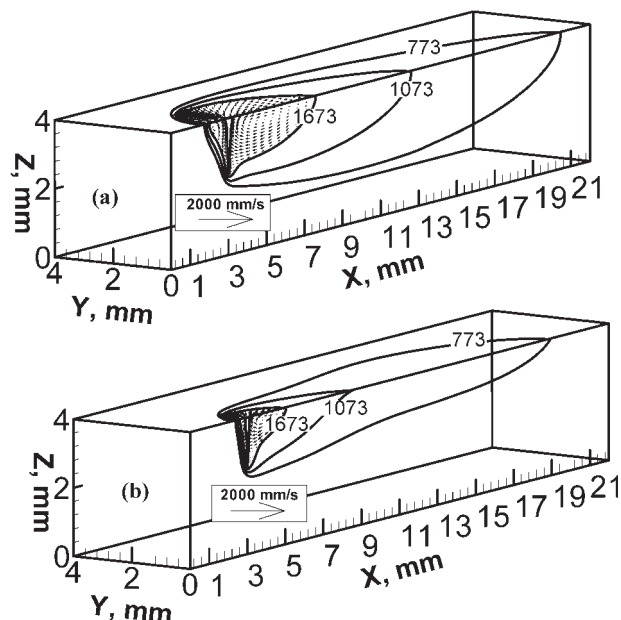
Figure 2a shows the calculated hybrid weld pool depth as a function of the distance between the arc electrode and laser beam. The figure shows that the penetration increases slightly at an optimal separation distance. In addition, increasing the arc current causes a small increase in the penetration depth of the weld pool. The experimental observations of Chen *et al.*² are shown in Figure 2b. The experimental and calculated results are in good agreement.

Figure 3 shows calculated weld pool velocity vectors (mm s^{-1}) and temperature (K) profiles for 900 W laser 60 A arc hybrid welds with two different separation distances, 3.5 and 7.6 mm. The welding direction is along the negative x -axis. Marangoni convection primarily dictates the fluid flow⁹ (Fig. 3a and b) and causes the weld pool to bulge towards the rear. The high energy density of the laser heat source results in the deep penetration of the weld pool. The maximum temperature experienced in the weld pools is 3100 K at the keyhole wall, i.e. the boiling point of the alloy. The boiling point is defined as the temperature at which the sum total of the partial pressures of the vaporised alloying elements is equal to ambient pressure (1 atm). When the separation distance is 3.5 mm (Fig. 3a), the arc and laser are acting at the same location. The arc in this case, although originally located 3.5 mm from the laser, is bending and rooting at the same location of the laser beam. The arc bending and contraction increases the penetration depth of the weld pool.

Increasing the distance between the arc electrode and laser beam beyond a critical distance results in tandem welding. Figure 3b depicts a tandem weld. The arc and laser are not interacting and are at two separate physical locations on the workpiece surface. The distance between the arc electrode and laser is 7.6 mm. The location of the 1073 and 773 K isotherms are shown in

Table 5 Arc radius used in heat transfer and fluid flow simulations to achieve measured results of Chen *et al.* when hybrid welding AISI 321 stainless steel

Measured heat source separation, mm	Arc radius, mm 60 A arc	Arc radius, mm, 120 A arc	Arc radius, mm, 180 A arc
3.5	0.39	0.55	0.6
4.6	0.32	0.5	0.49
5.4	0.39	0.38	0.47
6.5	0.39	0.47	0.44
7.6	4.16	0.43	0.38
8.2	4.16	0.52	0.44
9.2	4.16	0.52	0.45



3 Temperature and velocity profiles for hybrid welded AISI 321 stainless steel: a shows temperature and velocity profiles within weld pool and 1073 and 773 K isotherms; all of temperature values are in K; b temperature and velocity profiles when heat sources are separated by 7.6 mm

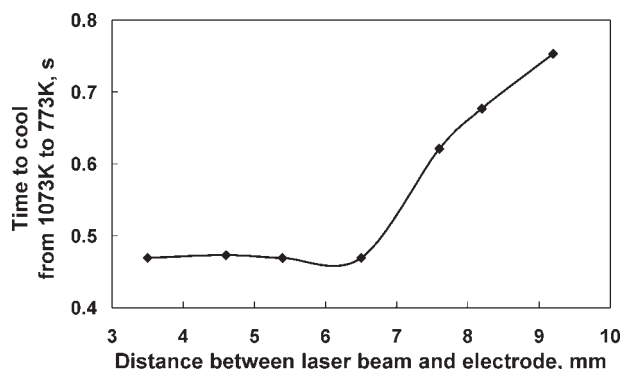
Fig. 3. The time to cool from 1073 to 773 K (800 to 500°C) and the cooling rate can be calculated by dividing the distance between the two contours where they intersect the x -axis by the welding speed. The separation distance between the heat sources affects the shape and relative distance between isotherms. When the separation distance increases from 3.5 to 7.6 mm, the cooling rate between 1073 and 773 K along the weld centreline at the top surface decreases from approximately 617 to 481 K s⁻¹. The cooling rate of the material was calculated by

$$R = \frac{\Delta T}{\Delta x} v \quad (14)$$

where R is the cooling rate in K s⁻¹, ΔT is the temperature difference (300 K), Δx is the distance between the 1073 and 773 K isotherms in millimetres, and v is the welding velocity in mm s⁻¹. The time to cool from 1073 to 773 K as a function of the heat source separation distance for the 60 A arc current hybrid welds is shown in Fig. 4. Beyond a critical separation distance, the cooling rate of the material along the weld centreline decreases significantly and the time to cool from 1073 to 773 K increases linearly as separation distance increases in the range considered. The cooling time from 1073 to 773 K increases as the distance between the 1073 and 773 K isotherms increases. The increase in distance between the isotherms results from the arc heat source being rooted behind the laser focal point, rather than at the same location. As the arc moves further away from the laser, it acts more as a post heat treatment process, which reduces the cooling rate of the weld pool.

Role of laser power level variation on weld pool geometry and fluid flow

Laser, GTA and hybrid bead-on-plate welds were performed on A131 structural steel with various laser

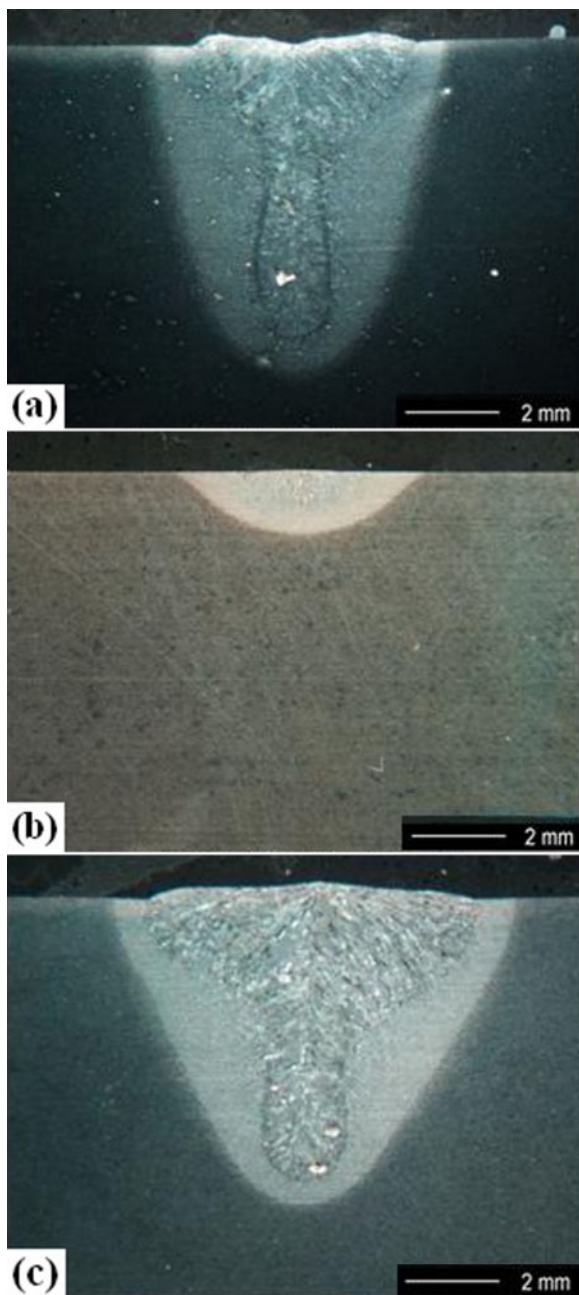


4 Time to cool from 1073 and 773 K in seconds as function of distance between arc electrode and laser beam

power levels, while a constant heat source separation distance was maintained. The results of the experiments were modelled by use of the three-dimensional heat transfer and fluid flow model. Figure 5 shows the experimentally observed weld cross-sections for laser (Fig. 5a), GTA (Fig. 5b), and hybrid (Fig. 5c) welds. The laser and hybrid welds were made using a 4.5 kW laser. A 191 A, 11 V arc was used in the case of the GTAW and 190 A, 12.3 V arc in the case of the hybrid weld. The welding velocity was 8.5 mm s⁻¹. The hybrid welding process results in a wider weld pool than laser or arc welding. However, there is minimal or no increase in weld pool depth in hybrid laser-arc welding over laser welding. The GTAW process results in much lower depth compared to laser or hybrid welds.

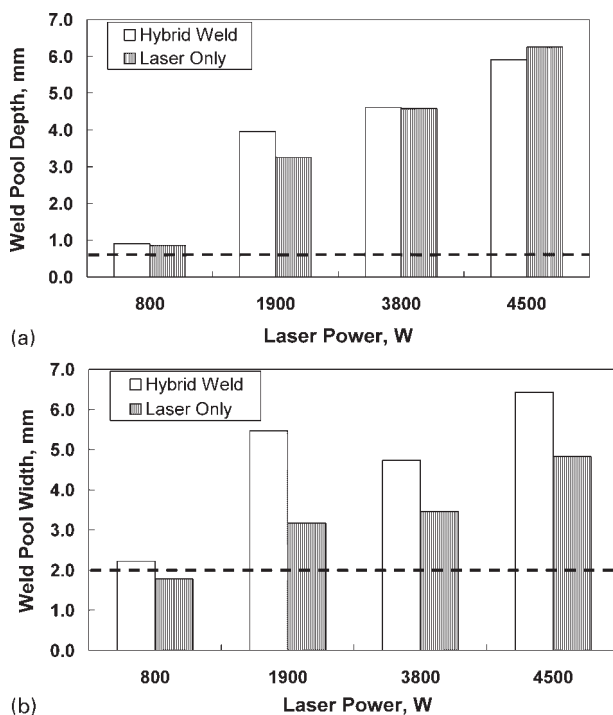
A comparison of GTA, laser and hybrid weld depths (Fig. 6a) and widths (Fig. 6b) is presented in Fig. 6. The weld dimensions for GTAW are depicted as dashed horizontal lines on the graphs. Figure 6a shows that the weld penetration depth is primarily a function of the laser power. The laser and hybrid welding processes offer deeper weld pool penetration than the GTAW process. However, the hybrid welding process does not result in a significant increase in weld pool penetration depth over lone laser welding. In the case of 4.5 kW hybrid weld, the weld pool depth is lower than that of the 4.5 kW laser weld due to the lack of an air knife to protect the focusing lens, which can affect the energy distribution of the laser beam. On the other hand, the hybrid welding process results in wider weld pools than lone laser or arc welding, as shown in Fig. 6b. Increased weld pool width is beneficial when attempting to bridge gaps present between welded sections and increase productivity.

The reason for these weld pool shapes is explained by the nature of the welding processes. The laser beam is a high energy density heat source which is very focused at the surface of the workpiece and results in deep penetration. The Marangoni force causes the weld pool to widen near the workpiece surface.^{62,78-80} The GTAW process results in strong electromagnetic and Marangoni (surface tension driven) forces.^{78,79,81} It will be shown later that the Marangoni force and the electromagnetic forces were of the same order for the conditions of the experiments.⁸² When both arc and laser are used, the amount of liquid metal generated by the two heat sources increases relative to lone arc or laser welding. Both the increase in the volume of liquid metal generated by the heat sources and strong Marangoni convection increase the width of the hybrid weld pool.



5 Weld cross-sections of A131 structural steel *a* laser welded, *b* arc welded, and *c* hybrid welded: for laser and hybrid welds, laser power is 4.5 kW; arc current and voltage are 191 A and 11 V for arc weld, and 190 A and 12.3 V for hybrid weld respectively; welding velocity was 8.5 mm s^{-1} for all welds

The fluid flow in the case of the laser, GTA, and hybrid welds is shown in Fig. 7. The welding velocity for all of the welds was 8.5 mm s^{-1} . The convective flow, arising from the Marangoni force during GTAW using an 11 V and 191 A arc, results in a shallow and wide weld pool shown in Fig. 7*a*. The fluid flow due to Marangoni convection along the surface of the weld pool (Fig. 7*b*) causes the top of the 1.9 kW laser weld pool to widen. The hybrid weld (Fig. 7*c*) was made using a 1.9 kW laser power level and a 185 A and 20 V arc. During hybrid welding, the additional heat input from combining the two heat sources causes more liquid to form and results in a larger weld pool. The depth of the weld pool is the same as the lone laser weld since the laser



6 *a* measured weld pool depth and *b* width as function of laser power for hybrid and lone laser welding; dashed line is weld pool depth and width achievable by lone GTAW

beam power level was the same. The increase in the hybrid weld pool width can be attributed to the increase in melting efficiency as observed in previous literature.^{20,41} The overall volume of the hybrid weld pool increases relative to the laser weld pool. Since the depth of the weld pool is relatively unchanged, the strong Marangoni convection at the top surface causes the additional liquid metal formed during hybrid welding to increase the weld pool width relative to lone laser welding.

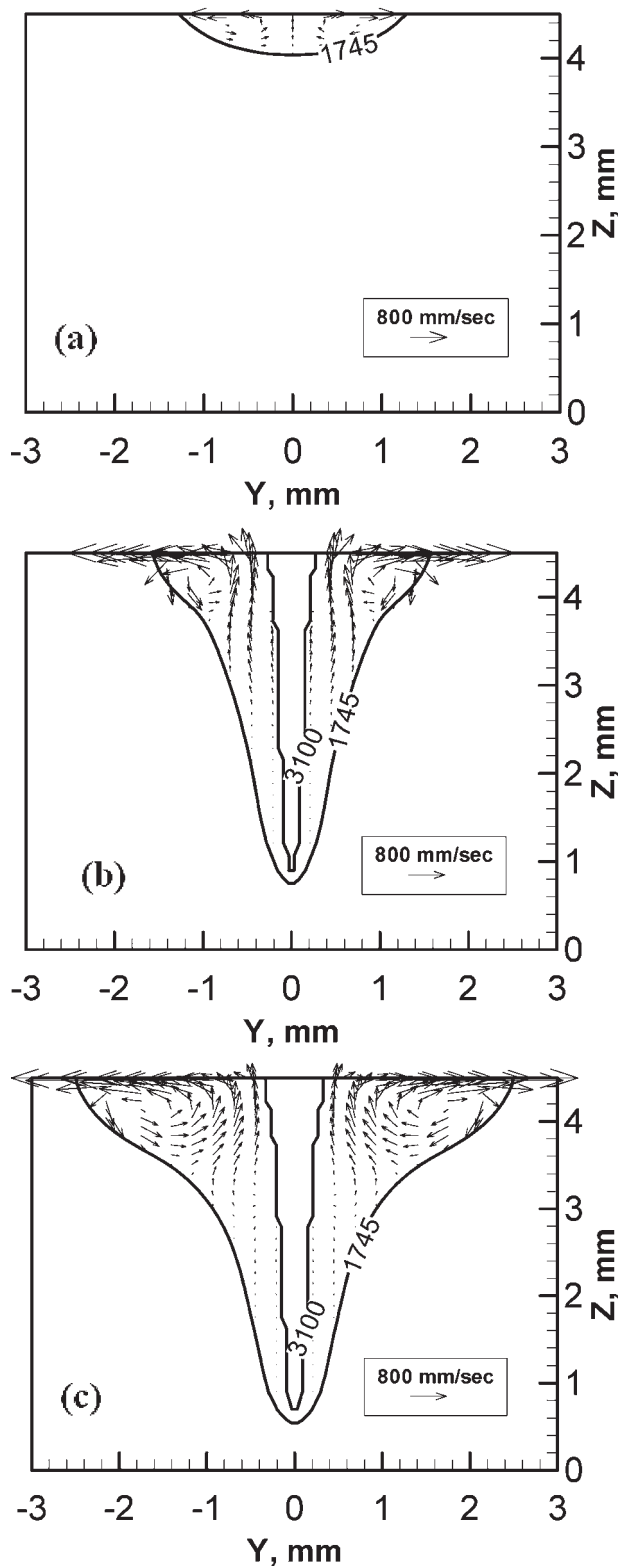
The dimensionless Peclet number is used to understand the significance of the role of heat transfer by convection relative to heat transfer by conduction⁶²

$$Pe = \frac{\text{convection}}{\text{conduction}} = \frac{UL}{\alpha} \quad (15)$$

where U is the characteristic velocity of the molten metal, L is a characteristic length (half of the weld pool width) and $\alpha (=k/\rho C_p)$ is the thermal diffusivity of the material ($1.43 \times 10^{-5} \text{ m}^2 \text{ s}^{-1}$). Table 6 shows the calculated Peclet numbers for the GTA, laser and hybrid A131 structural steel weldments. Since the Peclet number is much greater than 1, convection plays a significant role in the heat transfer process during GTA, laser and hybrid welding. When switching from laser to hybrid welding, the characteristic velocity of the molten metal increases, which can result in a more homogenous weld pool, especially when using filler metal.

The relative importance of the Marangoni and electromagnetic forces are given by the dimensionless magnetic and surface tension Reynolds numbers. The magnetic Reynolds number defines the ratio of the electromagnetic force to the viscous forces and is given by^{82,83}

$$Re_m = \frac{\text{electromagnetic}}{\text{viscous}} = \frac{\rho \mu_o \mu_r I^2}{4\pi^2 \mu^2} \quad (16)$$



7 Cross-sectional fluid flow in a GTA, b laser and c hybrid welds: isotherms are in units of Kelvin; laser power was 1.9 kW for both laser and hybrid welding; GTA weld was performed using 11 V and 191 A; hybrid weld was made using 185 A and 20 V arc

where ρ is the density of the material (7000 kg m^{-3}), μ_0 is the magnetic permeability of free space ($4\pi \times 10^{-7} \text{ N A}^{-2}$), μ_r is the relative permeability (1.0), I is the arc current ($\sim 190 \text{ A}$), and μ is the viscosity of the material ($5 \times 10^{-3} \text{ kg m}^{-1} \text{ s}^{-1}$). The magnetic Reynolds number in

the case of the hybrid or GTA welding of A131 structural steel for the conditions of the experiment is 3.2×10^5 . The surface tension Reynolds number defines the ratio of the surface tension (Marangoni) forces to the viscous forces and is given by^{82,83}

$$Re_s = \frac{\text{surface tension}}{\text{viscous}} = \frac{\rho L \Delta T \left| \frac{d\gamma}{dT} \right|}{\mu^2} \quad (17)$$

where L is a characteristic length ($2 \times 10^{-3} \text{ m}$), ΔT is the temperature difference between the peak temperature (3100 K) and the liquidus temperature (1745 K), and $d\gamma/dT$ is the temperature coefficient of surface tension ($-4.7 \times 10^{-4} \text{ N m}^{-1} \text{ K}^{-1}$). The surface tension Reynolds number in the case of hybrid welding for the conditions of experiment is 3.5×10^5 . The ratio of the magnetic and surface tension Reynolds numbers gives the relative importance of the electromagnetic to surface tension forces (Re_m/Re_s). The ratio of electromagnetic forces to surface tension forces is 0.9, which means that the two forces are of the same order.

In order to achieve the experimentally measured weld pool depth and width, the arc bending and contraction had to be included in the numerical model calculations. The arc radius for a 191 A arc with an arc length of 1.5 mm in the absence of metal vapours from another source like a keyhole was 1.0 mm. The values used for the heat source separation distance and the arc radius in the hybrid welding calculations are shown in Table 7. The data is ordered according to the laser power level of the particular hybrid weld. During the simulations of the weld pool temperature and fluid velocity profiles, it was observed that the amount of constriction of the arc radius primarily affected the weld pool penetration depth, while the separation distance affected the weld pool width. However, this observation has yet to be experimentally verified.

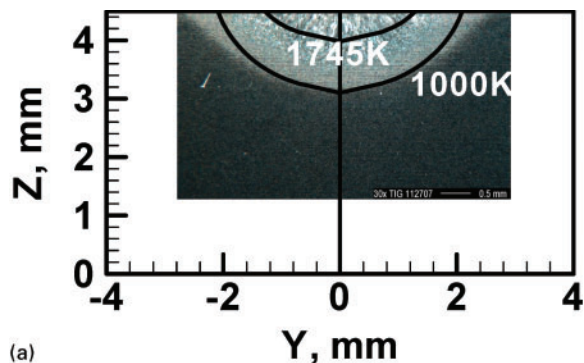
A comparison of the A131 structural steel GTA, laser and hybrid welding experimental and calculated results is shown in Figs. 8 and 9. Figure 8 shows GTA, laser and hybrid weld cross-sections. The calculated cross-section is overlaid on top of the micrograph. The dashed line shown in the calculated result is the 3100 K isotherm, which represents the keyhole wall. In addition to the weld pool solid/liquid boundary (1745 K isotherm), the HAZ/base metal boundary is shown by the

Table 6 Dimensionless Peclet number for GTAW, laser and hybrid welding

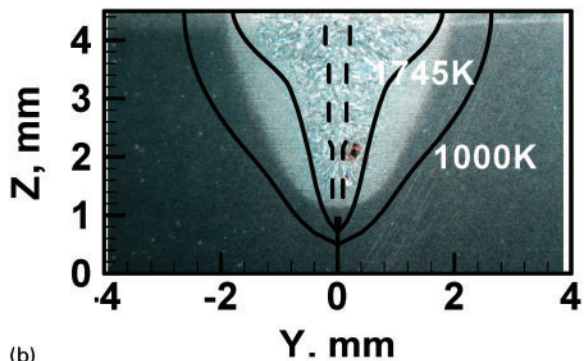
	GTAW	Laser	Hybrid
L, mm	2.0	3.0	4.0
u, mm s ⁻¹	250	300	400
Pe	35	63	112

Table 7 Separation distance and arc radius values used in numerical model in order to achieve experimentally observed hybrid weld pool width and depth: results are arranged by laser power level

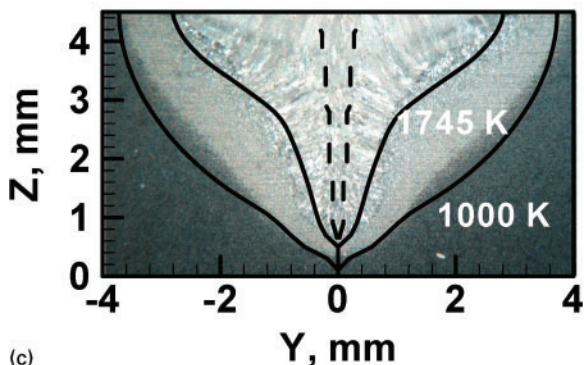
Laser power, W	Separation distance, mm	Arc radius, mm
4500	2	1
3800	0	0.9
1900	0.2	0.65
800	0.3	0.5



(a)



(b)



(c)

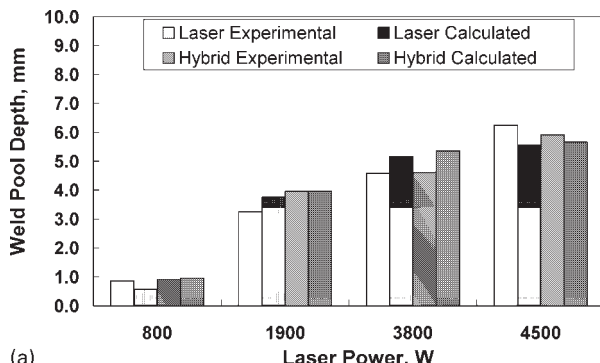
8 *a* GTA, *b* laser and *c* hybrid welded A131 structural steel cross-sections with calculated cross-section overlaid on top of experimental result: dashed isotherm is 3100 K isotherm, i.e. location of keyhole

1000 K isotherm. The laser power in the case of the hybrid and laser (Fig. 8*b*) welds was 1.9 kW. The GTA (Fig. 8*a*) weld was performed using a 191 A and 11 V arc. The arc current and voltage for the hybrid weld (Fig. 8*c*) was 185 A and 20 V respectively.

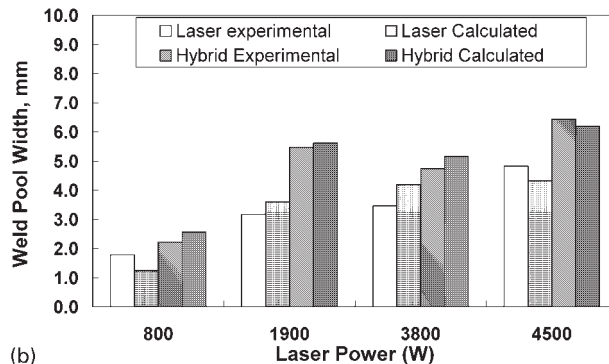
The calculated and measured results showed that the laser power level is the primary factor affecting weld pool penetration depth. The arc, in the case of hybrid welding, results in only a small increase in penetration depth. Figure 9*a* is a comparison of the calculated and measured laser and hybrid weld pool depths. The hybrid welding results show a minor increase in weld pool depth over lone laser welding. Weld pool width increases significantly when comparing hybrid to laser welding, which is shown in Fig. 9*b*. Increased weld pool width improves the ability to bridge gaps between components being welded, which is particularly important for welding large sections of material.

Summary and conclusions

A three-dimensional heat transfer and fluid flow model for hybrid laser/GTA welding has been proposed and



(a)



(b)

9 Comparison of calculated and measured laser and hybrid A131 structural steel weld geometry *a* shows depth and *b* indicates width

validated using experimental results. The model considers the enhanced absorption of laser beams due to multiple reflections inside the keyhole. It was found that when the inner heat source spacing becomes greater than a critical distance, the cooling rate of the molten weld pool increases significantly. In addition, in order to achieve the slight increase in the observed weld pool penetration depth at small separation distances between the arc and the laser, the arc must contract. The calculations showed that the arc contraction tended to affect weld pool depth, while the heat source separation distance tended to affect the weld pool width.

The hybrid welding process results in a similar weld pool penetration compared to lone laser welding. However, hybrid welding leads to a significant increase in weld pool width over lone laser welding and GTAW. The increase in weld pool width is the result of heat input from the arc and the heat transfer aided by strong Marangoni convection. Wider weld pools improve the ability of the hybrid welding process to allow for gaps between large welded sections of material without the necessity of additional bracing. Hybrid welding results in faster fluid flow than lone laser or arc welding due to the improved convection by the addition of an arc heat source. The arc heat source results in electromagnetic and increased Marangoni convection.

Acknowledgements

The authors would like to express sincere thanks to Dr. Todd A. Palmer, Dr. Shawn Kelly, Ed Good, Bill Rhoads, Chris Sills, Jay Tressler, Dr. Thomas J. Lienert, and Dr. Patrick Hochanadel for their interest and support.

References

1. C. Bagger and O. Flemming: *J. Laser Appl.*, 2004, **17**, 2–14.
2. Y. B. Chen, Z. L. Lei and L. Wu: *Sci. Technol. Weld. Join.*, 2006, **11**, 403–411.
3. M. El Rayes, C. Walz and G. Sepold: *Weld. J.*, 2004, **2004**, 147s–153s.
4. C. J. Page, T. Devermann, J. Biffin and N. Blundell: *Sci. Technol. Weld. Join.*, 2002, **7**, 1–9.
5. W. M. Steen: *J. Appl. Phys.*, 1980, **51**, 5636–5640.
6. J. Tusek and M. Suban: *Sci. Technol. Weld. Join.*, 1999, **4**, 308–311.
7. W. W. Duley: ‘CO₂ lasers effects and applications’; 1976, San Diego, CA, Academic Press, Inc.
8. R. Rai, G. G. Roy and T. DebRoy: *J. Appl. Phys.*, 2007, **101**, 11.
9. R. Rai, J. W. Elmer, T. A. Palmer and T. DebRoy: *J. Phys. D*, 2007, **40D**, 5753–5766.
10. R. Rai, S. M. Kelly, R. P. Martukanitz and T. DebRoy: *Metall. Mater. Trans. A*, 2008, **39A**, 98–112.
11. L.-M. Liu, G. Song, J.-F. Wang and G.-L. Liang: *Transactions of the Nonferrous Metals Society of China*, 2004, **14**, 550–555.
12. L. Liu, G. Song, G. Liang and J. Wang: *Mater. Sci. Eng. A*, 2005, **A390**, 76–80.
13. L. M. Liu, X. J. Liu and S. H. Liu: *Scripta Mater.*, 2006, **55**, 383–386.
14. P. L. Moore, D. S. Howse and E. R. Wallach: *Sci. Technol. Weld. Join.*, 2004, **9**, 314–322.
15. J. Kroos, U. Gratzke and G. Simon: *J. Phys. D*, 1993, **26D**, 474–480.
16. J. Kroos, U. Gratzke, M. Vicanek and G. Simon: *J. Phys. D*, 1993, **26D**, 481–486.
17. S. Tsukamoto, I. Kawaguchi, G. Arakane and H. Honda: *Sci. Technol. Weld. Join.*, 2001, **6**, 363–367.
18. M. von Allmen: ‘Laser-beam interactions with materials’; 1987, New York, NY, Springer-Verlag.
19. B. Hu and G. Den Ouden: *Sci. Technol. Weld. Join.*, 2005, **10**, 76–81.
20. B. Hu and G. Den Ouden: *Sci. Technol. Weld. Join.*, 2005, **10**, 427–431.
21. T. Jokinen and M. Karhu: *J. Laser Appl.*, 2003, **15**, 220–224.
22. S. Akbar and K. Etemadi: *Plasma Chem. Plasma P.*, 1997, **17**, 251–262.
23. G. J. Dunn and T. W. Eager: *Metall. Trans. A*, 1986, **17A**, 1865–1871.
24. K. C. Hsu, K. Etemadi and E. Pfender: *J. Appl. Phys.*, 1982, **54**, 1293–1301.
25. A. Mahrle and E. Beyer: *J. Laser Appl.*, 2006, **18**, 169–180.
26. G. Y. Zhao, M. Dassanavake and K. Etemadi: *Plasma Chem. Plasma P.*, 1990, **10**, 87–98.
27. X. Zhou and J. Herberlein: *J. Phys.*, 1998, **31**, 2577–2590.
28. M. Collur, A. Paul and T. DebRoy: *Metall. Trans. B*, 1987, **18B**, 733–740.
29. X. He, P. Fuerschbach and T. DebRoy: *J. Appl. Phys.*, 2003, **94**, 6949–6958.
30. X. He, P. Fuerschbach and T. DebRoy: *J. Phys. D*, 2003, **36D**, 3079–3088.
31. P. A. A. Khan and T. DebRoy: *Metall. Trans. B*, 1984, **15B**, 641–644.
32. M. M. Collur and T. DebRoy: *Metall. Trans. B*, 1989, **20B**, 277–286.
33. R. Miller and T. DebRoy: *J. Appl. Phys.*, 1990, **68**, 2045–2050.
34. K. Etemadi and E. Pfender: *Plasma Chem. Plasma P.*, 1985, **5**, 175–182.
35. K. Etemadi and E. Pfender: *Weld. J.*, 2007, **86**, 42–45.
36. C. M. Allen, G. Verhaeghe, P. A. Hilton, C. P. Heason and P. B. Prangnell: *Aluminum Alloys*, 2006, **519–521**, 1139–1144.
37. G. Casalino: *J. Mater. Process. Tech.*, 2007, **191**, 106–110.
38. H. W. Choi, D. F. Farson and M. H. Cho: *Weld. J.*, 2006, **85**, 174S–179S.
39. P. Denney and L. Brown: *Weld. J.*, 2002, **81**, 58.
40. M. Gao, X. Y. Zeng and Q. W. Hu: *Sci. Technol. Weld. Join.*, 2006, **11**, 517–522.
41. M. Gao, X. Zeng and Q. W. Hu: *J. Mater. Process. Technol.*, 2007, **184**, 177–183.
42. T. Graf and H. Staufner: *Weld. J.*, 2003, **82**, 42–48.
43. B. Hu and I. M. Richardson: *Mater. Sci. Eng. A*, 2007, **A459**, 94–100.
44. U. Jasnau, J. Hoffmann and P. Seyffarth: Proc. Int. Conf. on ‘Robotic welding’, Shanghai, China, 10–12 December 2002, Shanghai Jiao Tong University.
45. U. Jasnau, J. Hoffmann, P. Seyffarth: *Robotic Welding, Intelligence and Automation*, 2004, **299**, 14–24.
46. T. Jokinen, P. Jernstrom, M. Karhu, I. Vanttaja and V. Kujanpaa: Proc. 1st Int. Symp. on ‘High-power laser macroprocessing, Osaka, Japan, 27 May 2002, SPIE The International Society for Optical Engineering.
47. T. Kim, J. Kim, Y. Hasegawa and Y. Suga: *Mate. Sci. Forum*, 2004, **449**, 417–420.
48. T. Kim, Y. Suga and T. Koike: *JSME Int. J. A*, 2003, **46A**, 202–207.
49. M. Kutsuna and L. Chen: Proc. 1st Int. Symp. on ‘High-power laser macroprocessing, Osaka, Japan, 27 May 2002, SPIE The International Society for Optical Engineering.
50. L. Liming, J. Wang and G. Song: *Mater. Sci. Eng. A*, 2004, **A381**, 129–133.
51. L. Liu, G. Song and J. Wang: *Mater. Sci. Forum* 2005, **488**, 361–364.
52. L. Liu, X. Hao and G. Song: *Mater. Trans.*, 2006, **47**, 1611–1614.
53. L. M. Liu, G. Song and M. S. Chi: *Mater. Sci. Tech.*, 2005, **21**, 1078–1082.
54. Y. N. Liu and E. Kannatey-Asibu: *Trans. ASME*, 1993, **115**, 34–41.
55. G. L. Qin, Z. Lei and S. Y. Lin: *Sci. Tech. Weld. Join.*, 2007, **12**, 79–86.
56. H. Staufner: *Weld. J.*, 2007, **86**, 36–40.
57. Y. B. Chen, L. Q. Li, J. F. Fang and X. S. Feng: *J. Mater. Sci. Tech.*, 2003, **19**, 23–26.
58. M. H. Cho and D. F. Farson: *Weld. J.*, 2007, **86**, 253S–262S.
59. J. Zhou, W. H. Zhang, H. L. Tsai, S. P. Martin, P. C. Wang and R. Menassa: ASME International Mechanical Engineering Congress and Exposition, Washington DC, 16–21 November 2003, American Society of Mechanical Engineers.
60. A. Kaplan: *J. Phys. D*, 1994, **27D**, 1805–1814.
61. H. Zhao and T. DebRoy: *J. Appl. Phys.*, 2003, **93**, 10089–10097.
62. R. B. Bird, W. E. Stewart and E. N. Lightfoot: ‘Transport phenomena’; 1960, New York, John Wiley & Sons.
63. S. V. Patankar: ‘Numerical heat transfer and fluid flow’; 1980, New York, Hemisphere Publishing Corp.
64. A. D. Brent, V. R. Voller and K. J. Reid: *Numer. Heat Transfer*, 1988, **13**, 297–318.
65. V. R. Voller and C. Prakash: *Int. J. Heat Mass Transfer*, 1987, **30**, 1709–1719.
66. A. Kumar and T. DebRoy: *J. Appl. Phys.*, 2003, **94**, 1267–1277.
67. S. Kou and D. K. Sun: *Metall. Trans. A*, 1985, **16A**, 203–213.
68. K. Mundra, T. DebRoy and K. M. Kelkar: *Numer. Heat Transfer A*, 1996, **29A**, 115–129.
69. C. H. Kim, W. Zhang and T. DebRoy: *J. Appl. Phys.*, 2003, **94**, 2667–2679.
70. A. De and T. DebRoy: *J. Appl. Phys.*, 2004, **95**, 5230–5240.
71. A. De and T. DebRoy: *J. Phys. D*, 2004, **37D**, 140–150.
72. W. Pitscheneder, T. DebRoy, K. Mundra and R. Ebner: *Weld. J.*, 1996, **75**, 71s–80s.
73. H. Zhao and T. DebRoy: *Metall. Mater. Trans. B*, 2001, **32B**, 163–172.
74. B. E. Launder and D. B. Spalding: ‘Lectures in mathematical model of turbulence’; 1972, London, Academic Press.
75. D. C. Wilcox: ‘Turbulence modeling for CFD’; 1993, CA, DCW industries.
76. T. A. Palmer, J. W. Elmer, R. Pong and M. D. Gauthier: ‘Welding stainless steels and refractory metals using diode-pumped continuous wave Nd:YAG lasers’, UCRL-TR-206885, Lawrence Livermore National Laboratory, 2004.
77. N. S. Tsai and T. W. Eager: *Metall. Trans. B*, 1985, **16B**, 841–846.
78. T. DebRoy and S. A. David: *Rev. Modern Phys.*, 1995, **67**, 85–112.
79. S. Kou: ‘Welding metallurgy’, 13–62; 2003, New York, John Wiley & Sons, Inc.
80. D. A. Schauer, W. H. Giedt and S. M. Shintaku: *Weld. J.*, 1978, **57**, 127s.
81. J. F. Lancaster: ‘The physics of welding’, 9–29; 1986, New York, Pergamon Press.
82. W. Zhang, G. G. Roy, J. W. Elmer and T. DebRoy: *J. Appl. Phys.*, 2003, **93**, 3022–3033.
83. G. M. Oreper and J. Szekely: *Metall. Trans. A*, 1987, **18A**, 1325.
84. X. He, T. Norris, P. Fuerschbach and T. DebRoy: *J. Phys. D*, 2006, **39D**, 1257–1266.
85. P. Sahoo, T. DebRoy and M. J. McNallan: *Metall. Trans. B*, 1988, **19B**, 483–491.
86. X. He, J. Elmer and T. DebRoy: *J. Appl. Phys.*, 2005, **97**, 84909–84917.

87. P. Mouroulis and J. MacDonald: 'Geometrical optics and optical design'; 1997, Cambridge, UK, Oxford University Press.

Appendix

The keyhole wall angle at a particular depth is given by^{60,61}

$$\tan \theta = \frac{I_c}{I_a - I_v} \quad (\text{A1})$$

where I_c is the heat radially conducted from the keyhole wall into an infinite plate, I_a is the locally absorbed beam energy flux, and I_v is the evaporative heat flux. I_c is determined using two-dimensional temperature fields in an infinitely large plate with respect to a linear heat source. The heat conduction term is defined by

$$I_c = -\lambda \frac{\partial T(r, \varphi)}{\partial r} \quad (\text{A2})$$

where λ is the thermal conductivity, T is the temperature, (r, φ) describes a location in terms of a radial distance and angle perpendicular to the line source or origin, where $\varphi=0$ at the front keyhole wall and $\varphi=\pi$ at the rear keyhole wall. The two-dimensional temperature field term for the heat conducted radially from the keyhole walls into the infinitely large plate is given by⁸⁶

$$T(r, \varphi) = Ta + \frac{P'}{2\pi\lambda} K_0(\Omega r) e^{-\Omega r \cos \varphi} \quad (\text{A3})$$

where T_a is the ambient temperature, P' is the power per unit depth, $K_0()$ is the solution of the second kind zero-order modified Bessel function, $\Omega = v/2\kappa$, where v is the welding velocity, and κ is the thermal diffusivity. The absorption of the arc and laser beam is accounted for by the locally absorbed heat source flux defined as⁶¹

$$I_a = e^{-\beta l} \left[1 - (1 - \alpha)^{1 + \pi/4\theta} \right] I_o + I_{a,o} \eta \exp \left[-f_a \left(\frac{D_{LA} \pm r}{r_a} \right)^2 \right] \quad (\text{A4})$$

where β is the inverse Bremsstrahlung absorption coefficient of the plasma generated by the laser, α is the absorption coefficient of the workpiece material, θ

is the average angle between the keyhole wall and the incident beam axis, I_o is the local incident laser beam intensity that varies as a function of depth and radial distance, $I_{a,o}$ is the peak intensity of the arc, η is the arc efficiency ($\sim 0.25-0.7$), r_a is the arc radius, f_a is the arc energy distribution factor, r is the distance from the laser line source to the keyhole front or rear wall, and D_{LA} is the distance between the heat sources. The sign of r varies in order to calculate the distance between the arc location and the front and rear keyhole walls. For example, the distance between the arc location and keyhole front wall is calculated by adding r to D_{LA} , and the distance between the keyhole rear wall and arc heat source is calculated by subtracting r from D_{LA} . If the order in which the heat sources proceed over the workpiece is reversed, D_{LA} will become negative. The local incident laser beam intensity I_o is defined as

$$I_o = I_{fol} \alpha \left(\frac{r_{fo}}{r_f} \right)^2 \exp \left(-f_1 \frac{r^2}{r_f^2} \right) \quad (\text{A5})$$

where I_{fol} is the peak intensity of the laser at the focal plane, r_{fo} is the beam radius at the focal plane, f_1 is the laser energy distribution factor, and r_f is the local beam radius. The peak laser and arc intensities are defined by^{61,87}

$$I_{fol} = \frac{2P}{\pi r_{fo}^2} \quad (\text{A5a})$$

$$I_{a,o} = \frac{P}{2\pi r_a^2} \quad (\text{A5b})$$

where P is the nominal power of the heat source and r_a is the arc radius. The local beam radius (r_f) as a function of the depth (z) is defined by^{61,87}

$$r_f = r_{fo} \left[1 + \left(\frac{z + z_o}{2r_{fo}f/d_b} \right)^2 \right]^{1/2} \quad (\text{A5c})$$

where z_o is the beam defocusing, f is the laser beam focal length, and d_b is the diameter of the laser beam on the laser focusing lens.